Research Article Vol. 30, No. 25 / 5 Dec 2022 / *Optics Express* 44769

Optics EXPRESS

Generalized and wavelength-dependent temperature calibration function for multipoint regenerated fiber Bragg grating sensors

FABIAN BUCHFELLNER,[1,*] ANDREA STADLER,[1] QIANG BIAN,[1,2] MAXIMILIAN HENNESEN,[1] ANDREAS ZEISBERGER,[3] ALEXANDER W. KOCH,[2] AND JOHANNES ROTHS[1]

[1] *Photonics Laboratory, Munich University of Applied Sciences, 80335 Munich, Germany*
[2] *Institute for Measurement Systems and Sensor Technology, Technical University of Munich (TUM), 80333 Munich, Germany*
[3] *MTU Aero Engines AG, 80995 Munich, Germany*
[*] *fabian.buchfellner0@hm.edu*

Abstract: A new calibration methodology for regenerated fiber Bragg grating (RFBG) temperature sensors up to 700 °C is proposed and demonstrated. A generalized, wavelength-dependent temperature calibration function is experimentally determined that describes the temperature-induced wavelength shifts for all RFBG sensor elements that are manufactured with the same fabrication parameters in the wavelength range from 1465 nm to 1605 nm. Using this generalized calibration function for absolute temperature measurements, each RFBG sensor element only needs to be calibrated at one reference temperature, representing a considerable simplification of the conventional calibration procedure. The new calibration methodology was validated with 7 RFBGs, and uncertainties were found to be compliant with those of Class 1 thermocouples ($<$ ±1.5 K or $<$ $\pm0.4\%$ of the measured temperature). The proposed calibration technique overcomes difficulties with the calibration of spatially extended multipoint RFBG sensor arrays, where setting up an adequate calibration facility for large sensor fibers is challenging and costly. We assume that this calibration method can also be adapted to other types of FBG temperature sensors besides RFBGs. An accurate and practical calibration approach is essential for the acceptance and dissemination of the fiber-optic multipoint temperature sensing technology.

1. Introduction

Temperature can be regarded as the most widely recorded parameter in industrial measurement technology. Particularly, for many applications, detecting high temperatures and temperature distributions above 500 °C still pose unsolved challenges. Temperature control and monitoring are often critical regarding the safe operation, system efficiency, energy consumption, and product quality of various industrial processes and plants. If suitable solutions can be found, this will stimulate innovations in energy, mobility, material processing, and other industries. Conventional high-temperature measurement is often conducted with thermocouples for which extensive experience and standards exist. For instance, the maximum measurement error for Class 1 non-calibrated thermocouples described in European standard IEC 60584 is ±1.5 K or ±0.4% of the temperature measurement value (the larger value accounts) [1]. Alternative technologies for temperature sensors must fulfill or even outperform these tolerances to find serious attention in industry.

In recent years, fiber-optical temperature sensors have been intensively studied due to their immunity to electromagnetic interference, comparably small dimensions and thermal mass, and chemical stability. Especially, multipoint temperature sensing with fiber Bragg gratings (FBGs) opens additional inherent benefits due to their wavelength multiplex capability that permits the

#470093 https://doi.org/10.1364/OE.470093
Journal © 2022 Received 11 Jul 2022; revised 13 Oct 2022; accepted 14 Nov 2022; published 23 Nov 2022

fast acquisition of temperature profiles with limited cabling efforts. With the growing industrial interest in FBG-based high-temperature sensing, the Association of German Engineers (Verein Deutscher Ingenieure, VDI) recently published the recommendation 'VDI/VDE 2660 Paper 2' on measurement terminology and declaration of uncertainties [2].

High-temperature resistant FBGs can be subdivided into regenerated FBGs (RFBGs) and FBGs inscribed with a femtosecond laser (fs-FBGs). Regenerated FBGs are based on Type-I seed FBGs that have been inscribed into hydrogen-loaded optical fibers using nanosecond UV pulses and a phase mask [3]. During annealing of a seed grating for several hours at high temperatures, the seed vanishes, and a regenerated FBG (RFBG) emerges. Although the RFBG shows a significantly lower reflectivity than the initial grating, its reflectivity remains stable in further temperature cycles up to the temperature of the regeneration process [4]. The thermal treatment of RFBGs also reduces wavelength drifts at elevated temperatures, where typical values are in the order of ~10 pm/year (~1.0 K/year) at 500 °C [5]. Contrarily, fs-FBGs are fabricated with femtosecond laser pulses either with a phase mask [6] or point-by-point [7,8]. Such gratings have been reported for high-temperature sensing, intrinsically withstanding temperatures up to 1000 °C [9,10]. Fs-FBGs are not limited to Ge-doped and H_2-loaded optical fibers but suffer from undesired polarization effects [11] and scattering losses [12] that reduce accuracy and also exhibit even larger temperature drift rates when operated without pre-annealing [10].

Numerous real field experiments using high-temperature stable FBGs have been performed under different harsh environmental conditions. For instance, the mapping of temperature distributions in chemical reactors and power production facilities such as gas turbines, combustors, or solar power plants has been studied [5,13–21]. Further, the deployment under strong radiation such as in fusion devices has been reported [22–28]. FBGs have also been integrated into aluminum [29–31] and copper [32] cast parts for temperature and strain measurements during solidification. A summary of field experiments with further information on FBG-Type, spectral range, and maximum temperature is given in Table 1.

Table 1. Selection of accomplished field experiments in FBG-based high-temperature sensing.

Research group	Application field + Reference	Sensor type	Approximate spectral range [nm]	Approximate maximum temp. [°C]
Mihailov et al. (Canada)	- Entrained-flow gasifier and fluidized bed combustor [17,18]	Multi-fs-FBG	1512–1583	1025
	- Gas turbine combustion simulator [16]	Multi-fs-FBG	1512–1583	1000
	- High pressure combustor [15]	Multi-fs-FBG	1512–1583	900
Laffont et al. (France)	- Sodium-coolant of nuclear reactor [26,27]	Multi-RFBG	1531–1551	500
	- Fusion device [25,28]	Multi-RFBG	1512–1582	830
	- Fusion device [24]	Multi-fs-FBG	1470–1600	1170
Chen et al. (USA)	- Nuclear test reactor [22,23]	fs-FBG	1530	640
Xia et al. (USA)	- Coal gasification [20]	Multi-RFBG	1517–1564	1200
	- Gas turbine [21]	Multi-RFBG	1530–1573	450
Rodriguez-Garrido et al. (Spain)	- Central receiver solar power plant [19]	Multi-fs-FBG	1500–1581	570
Roths et al. (Germany)	- Aluminum casting and structural health monitoring [29–31]	Multi-RFBG	1540–1555	650
	- Copper casting [32]	Multi-RFBG	1540–1560	1150
	- Chemical reactor [5,14]	Multi-RFBG	1533–1558	500
	- Gas turbine [13,14]	Multi-RFBG	1533–1558	500

The potential for further application fields is large but mainly limited by irreversible Bragg wavelength drifts induced by high temperatures [10] or large neutron fluxes such as 1.2×10^{14} n cm^{-2} s^{-1} [22]. Another challenge of using large multipoint sensors is to establish an appropriate calibration procedure to achieve low measurement uncertainty, which is necessary to compete with thermocouples. The large spatial extent of up to several meters of the fiber optical sensor arrays makes the construction of a precise calibration facility with sufficient temperature homogeneity at temperatures up to ~700 °C difficult and expensive.

In this study, we propose and demonstrate a new calibration methodology for multipoint RFBGs that overcomes the above-mentioned issue with the calibration of spatially large RFBG sensor arrays. By means of this methodology, a generalized, wavelength-dependent temperature calibration function could be derived and applied. After determining the Bragg wavelength only at one reference temperature near room temperature, the generalized temperature calibration function can be applied to each RFBG sensor element that has been fabricated similarly. Therefore, we investigated 15 RFBGs, each at a different wavelength in the spectral range from 1465 nm to 1605 nm. The generalized, wavelength-dependent calibration function was derived with 8 of the 15 RFBGs by measuring their temperature- and wavelength-dependent responses from room temperature up to 700 °C. This generalized function was validated with the other 7 RFBGs, and the resulting uncertainties were comparable with those of Class 1 thermocouples. Hence, the proposed calibration technique overcomes difficulties with the calibration of spatially large multipoint RFBG sensor arrays and additionally considers the wavelength dependence of the RFBG temperature coefficients. We assume that this calibration method can also be adapted for fs-FBGs. An accurate and practical calibration approach is essential for the industrial deployment of fiber-optic multipoint temperature sensing.

2. Theory

In this chapter, the known theories on the temperature dependence of the Bragg wavelength are briefly reviewed in order to clarify the simplifications made for the generalized calibration function proposed here. The Bragg wavelength $\lambda_B(\vartheta, \lambda)$ for the first-order FBG diffraction wavelength is given by [3]

$$\lambda_B(\vartheta, \lambda) = 2\ n_{\mathrm{eff}}(\vartheta, \lambda)\ \Lambda(\vartheta), \tag{1}$$

where $n_{\mathrm{eff}}(\vartheta, \lambda)$ denotes the effective refractive index (RI) as a function of wavelength and temperature, and $\Lambda(\vartheta)$ denotes the temperature-dependent grating period. Temperature ϑ is stated in °C throughout this work. Standard optical fibers (SMF28) have a Ge-doped silica core (~3.5 mol.% [33]) but pure silica cladding. Under high-temperature conditions, nonlinear temperature responses have been found for the thermo-optic coefficient (TOC, temperature coefficient of the RI) [34] and the coefficient of thermal expansion (CTE) [35], while the temperature-induced RI change typically dominates the thermal expansion effect.

RIs are associated with polarizabilities of optical materials. The Sellmeier equations are a broadly accepted form to express the RI as a function of wavelength. These equations are derived from the Lorentz-Lorenz oscillator model, where the input parameters are resonance wavelengths and oscillation strengths at different resonance poles of the material system [36]. For SMF28 fibers, a 3-pole Sellmeier model (2 poles in UV, 1 pole in IR) has shown sufficiency, where the resonance wavelengths and oscillator strengths at room temperature (RT) can be derived from Fleming's dispersive model for binary materials due to balancing of $\mathrm{GeO_2}$ and $\mathrm{SiO_2}$ properties by means of molar fractions [37].

To extend the RI to a function of both wavelength and temperature, the oscillator strengths and resonance wavelengths can be considered as functions of temperature [38,39]. In literature, simplified Sellmeier models can be found that only express the oscillator strengths $\chi_{UV,i}(\vartheta)$ and resonance wavelengths $\lambda_{UV,i}(\vartheta)$ in the UV domain as functions of temperature, leading to

$$n(\lambda,\ \vartheta)^2 - 1 = \sum_{i=1}^{2} \chi_{UV,i}(\vartheta)\frac{\lambda^2}{\lambda^2 - \lambda_{UV,i}^2(\vartheta)} + \chi_{IR}\frac{\lambda^2}{\lambda^2 - \lambda_{IR}^2}, \tag{2}$$

where λ is the wavelength of the propagating wave. $\chi_{UV,i}(\vartheta)$ and χ_{IR} denote the oscillator strengths, and $\lambda_{UV,i}(\vartheta)$ and λ_{IR} the resonance wavelengths in the UV and IR, respectively [36,38–41].

Apparently, the Sellmeier model introduced in Eq. (2) implies that the RI yields a nonlinear function of temperature and wavelength. When light is guided within an optical fiber, the wavelength and temperature dependence of the effective RI is determined not only by the RI for the core and cladding materials but also by the wavelength-dependent confinement factor and, due to the photo-elastic effect, by thermal stress between cladding and core.

Taking reference to a temperature ϑ_0 and wavelength λ_0, for instance, at 0 °C, the effective RI $n_{\text{eff}}(\vartheta, \lambda)$ at temperature ϑ can be expressed as

$$n_{\text{eff}}(\vartheta, \lambda) = n_{\text{eff}}(\vartheta_0, \lambda_0)\left[1 + \frac{\Delta n_{\text{eff}}(\vartheta, \lambda)}{n_{\text{eff}}(\vartheta_0, \lambda_0)}\right], \tag{3}$$

with $\Delta n_{\text{eff}}(\vartheta, \lambda)$ being the nonlinear temperature-induced change of the effective RI. The Bragg wavelength of an FBG at 0 °C will be defined here as its ‘offset wavelength’

$$\lambda_0 \equiv 2\ n_{\text{eff}}(\vartheta_0, \lambda_0)\ \Lambda(\vartheta_0). \tag{4}$$

Moreover, Bachmann et al. [35] have reported nonlinear thermal expansion of silica glass. Thermal expansion of the optical fiber elongates the FBG and increases the grating period according to

$$\Lambda(\vartheta) = \Lambda_0\left[1 + \int_{\vartheta_0}^{\vartheta} \alpha_\Lambda(\tilde{\vartheta})\, d\tilde{\vartheta}\right] = \Lambda_0\left[1 + \frac{\Delta\Lambda(\vartheta)}{\Lambda_0}\right], \tag{5}$$

where Λ_0 is the grating period at $\vartheta_0 = 0$ °C, $\alpha_\Lambda(\vartheta)$ is the nonlinear CTE, and $\Delta\Lambda(\vartheta)$ is the temperature-dependent elongation. Using this definition and substituting Eq. (3)–(5) into (1) yields

$$\lambda_B(\vartheta, \lambda) = \lambda_0\left[1 + \frac{\Delta n_{\text{eff}}(\vartheta, \lambda)}{n_{\text{eff}}(\vartheta_0, \lambda_0)}\right]\left[1 + \frac{\Delta\Lambda(\vartheta)}{\Lambda(\vartheta_0)}\right]. \tag{6}$$

Here, we introduce the simplifying assumption that the temperature-induced relative RI change is independent of wavelength with $\Delta n_{\text{eff}}(\vartheta, \lambda) \cong \Delta n_{\text{eff}}(\vartheta)$ due to $\Delta n_{\text{eff}}(\vartheta) \gg \Delta n_{\text{eff}}(\lambda)$ that leads to

$$\lambda_B(\vartheta, \lambda_0)\ \cong\ \lambda_0\left[1 + \frac{\Delta n_{\text{eff}}(\vartheta)}{n_{\text{eff}}(\vartheta_0)}\right]\left[1 + \frac{\Delta\Lambda(\vartheta)}{\Lambda(\vartheta_0)}\right]. \tag{7}$$

Neglecting higher-order terms with $\Delta n_{\text{eff}}(\vartheta)\Delta\Lambda(\vartheta)$, the temperature-induced Bragg wavelength shift of a FBG, $\Delta\lambda_B(\vartheta, \lambda_0)$, with offset wavelength λ_0 can be formulated as

$$\Delta\lambda_B(\vartheta, \lambda_0) = \lambda_B(\vartheta, \lambda_0) - \lambda_0 = \lambda_0\left[\frac{\Delta n_{\text{eff}}(\vartheta)}{n_{\text{eff}}(\vartheta_0)} + \frac{\Delta\Lambda(\vartheta)}{\Lambda(\vartheta_0)}\right] \cong\ \lambda_0 \sum_{i=1}^{n} B_i\, \vartheta^i. \tag{8}$$

The summation in the brackets of Eq. (8) only depends on temperature and can be approximated by a multiple order polynomial function with coefficients B_i, which is typically used to describe the temperature-induced shift of the Bragg wavelengths [2]. Hence, this approximation for a generalized, wavelength-dependent calibration function with nonlinear temperature response assumes that the temperature dependence of the effective refractive index does not depend on wavelength, which needs to be verified experimentally, as addressed in the subsequent sections.

3. RFBG sensor fabrication and calibration

3.1. Seed grating inscription and regeneration procedure

For the aimed demand of calibration precision and reproducibility throughout this work, it was crucial to maintain all fabrication parameters properly among all investigated FBGs. The setup for Type-I FBG writing is shown in Fig. 1. A KrF excimer laser with an emission wavelength of 248 nm and the phase mask principle [3] provided the required interference pattern for seed grating inscription into hydrogen-loaded standard single-mode fibers (SMF28). Prior to inscription, the fibers had been subjected to a hydrogenation process using pure hydrogen at a pressure of 100 bar at room temperature (RT) for two weeks. With a cylindrical lens, the beam was focused onto the fiber axis, whereas an aperture limited the beam width to achieve a grating length of $L = 900\ \mu m$. In total, 15 uniform seed gratings were fabricated with a fixed number of 7500 shots with 5 mJ per pulse at a repetition rate of 100 Hz. Each of the 15 seed FBGs had a bandwidth of $\delta\lambda \approx 2\ nm$ (measured between the first zeros on either side of the main lobe) with different central wavelengths between 1465 nm and 1605 nm (140 nm), and with a spectral separation of 10 nm between consecutive FBGs. Each grating was written in a separate single fiber, where the acrylate coatings had been chemically removed using acetone before inscription. A four-channel Hyperion si255 interrogator (Luna Inc., Roanoke, USA) acquired the spectra with 8 pm sample spacing. Figure 2(a) (left ordinate) shows three exemplary spectra of the 1465 nm (blue), 1545 nm (green) and 1605 nm (red) seed FBGs.

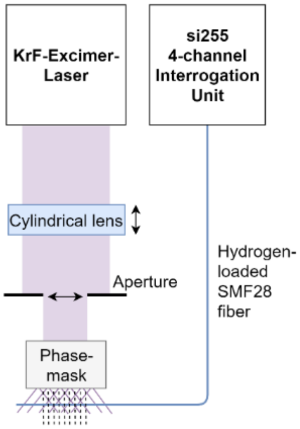

Fig. 1. Inscription setup (top view) used for Type-I seed grating fabrication.

Exposition to an annealing procedure activates regeneration and high-temperature stability of the FBGs [4]. Therefore, the gratings were placed inside a calibration furnace (Pegasus Plus 1200 S, Isothermal Technology Ltd., Merseyside, UK), which was used for both regeneration and temperature calibration. Figure 2(c) shows a schematic of the calibration furnace. The metal block of the device had a blind hole with an inner diameter of 8 mm, a depth of 80 mm, and an insulation thickness of 50 mm. Temperature control was performed using internally mounted power circuits and an internal thermocouple (TC). Temperature homogeneity was ensured at the lower 10 mm of the blind hole. Hence, fibers were angle cleaved at ~1 mm behind the gratings to prevent signals from undesired etalon effects. The FBGs were then suspended into the homogeneous area of the bore hole without touching the furnace bottom. A calibrated Type-R platinum TC acquired the reference temperature and was placed together with the seed gratings in the same blind hole. According to the calibration certificate, the maximum uncertainty of the reference TC was ±2.0 K at 700 °C [42].

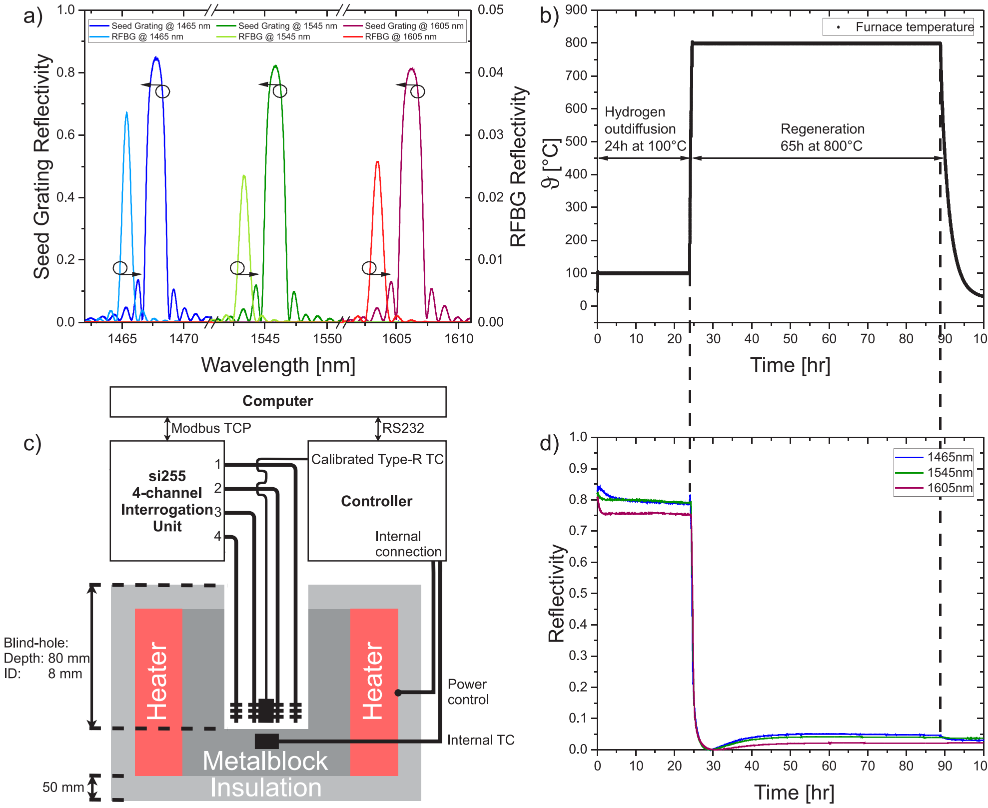

Fig. 2. a) Spectra of three exemplary gratings obtained before and after the annealing process with nominal wavelengths of 1465 nm (red), 1545 nm (green) and 1605 nm (blue). After thermal annealing, RFBGs emerged with high temperature stability, but decreased reflectivities, decreased spectral widths, and blue-shifted Bragg wavelengths. b) Temperature profile over time during the annealing procedure, subdivided into a hydrogen out-diffusion period at 100 °C for 24 h and a regeneration period at 800 °C for 65 h. c) Schematic of the metal block calibration furnace used for thermal annealing of seed gratings and calibration of RFBGs. For temperature reference, a calibrated Type-R TC was placed together with the RFBGs at ~1 mm above the bottom of the blind hole. d) Reflectivities as a function of time for the three exemplary FBGs. After approximately 30 h, 6 h after launching the regeneration, the FBG reflectivities decayed and emerged again during regeneration. Constant levels indicated successful regeneration and stable gratings.

Figure 2(b) depicts the deployed temperature profile during annealing. This procedure was subdivided into a pre-annealing at 100 °C for 24 h to ensure out-diffusion of remaining hydrogen within the FBG. Consecutively, the furnace temperature was increased to 800 °C, where the regeneration with a duration of 65 h was accomplished. The transition time from 100 °C to 800 °C was around 40 minutes, and therefore, much shorter than the total duration of the regeneration cycle. Hence, the annealing can be assumed as almost isothermal. Temperatures and peak fitted wavelengths were continuously recorded and saved with 0.2 Hz.

Successful regeneration processes were checked by observing the reflectivity profiles over time, as shown in Fig. 2(d) for the previously mentioned three exemplary gratings. Initially, the reflectivities fluctuated slightly, indicating hydrogen out-diffusion. After 30 h – approx. 6 h after increasing the furnace temperature to 800 °C – the FBG signals vanished entirely.

Thereupon, new reflectivities emerged and grew to constant levels, indicating successful regeneration. Spectra of the manufactured RFBG temperature sensors are shown in Fig. 2(a) (right ordinate). Due to the thermal treatment, reflectivities decayed to approximately 5% of the initial seed grating strength. However, the SNR was still sufficient for proper processing of the wavelength-encoded signals. The long annealing time of 65 hours served to reduce the temperature drift of the RFBG sensors.

Irreversible blue-shifting wavelength drifts were commonly observed during thermal annealing in the range of 2–3 nm for the produced RFBGs. Dutz et al. [14] considered that the thermally induced drift at high temperatures may be caused by stress relaxation of frozen-in stresses during fiber production and compaction mechanisms in the complex fiber structure.

3.2. Calibration setup

Consecutively after regeneration, the fibers remained in the same furnace, and the calibration process was started. Figure 3(a) shows the temperature cycles on the left ordinate and one exemplary wavelength on the right ordinate as functions of time. The furnace was stabilized at seven set points between 150 °C and 700 °C, whereby in total, two cycles of heating and cooling were performed. Each step was held for 90 minutes to ensure temperature equilibrium. Averaging the 10 final minutes at each step, i.e., 120 data points measured with 0.2 Hz of both the reference temperature and wavelengths allowed the determination of the temperature vs. wavelength relationship. The drift of the Bragg wavelengths during calibration was less than 2 pm, which corresponds to a temperature drift of less than 0.2 °C, which can be neglected here in the context of the furnace uncertainties.

The metal block calibration furnace cannot be stabilized at a temperature near RT. Hence, to determine the Bragg wavelength at RT, we placed the fibers additionally inside a custom-built Peltier-driven calibration device, which was stabilized at approximately 20 °C. As shown in Fig. 3(b), the controlled copper block of this device had five bores. Four were intended for the RFBG sensors and a larger one for a calibrated PT100 resistive temperature sensor measured by a multimeter. According to the calibration certificate, the PT100 had an uncertainty of 0.08 K at RT [43]. Wavelength and temperature data obtained over 10 minutes were averaged and included in the calibration data set.

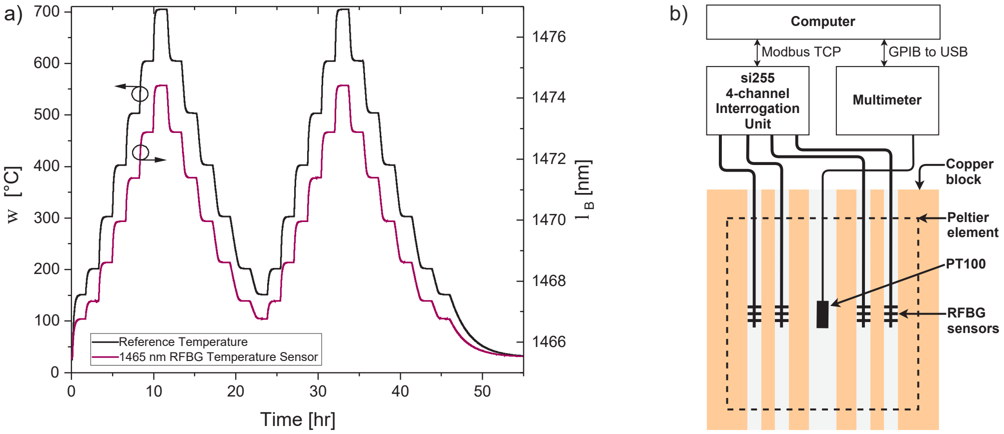

Fig. 3. a) Temperature profile during calibration (black, left ordinate) and an exemplary 1465 nm RFBG temperature sensor's wavelength profile (red, right ordinate). b) Schematic of a Peltier-driven calibration device for wavelength calibration data acquisition near RT. A calibrated PT100 resistive sensor measured reference temperatures with an uncertainty of ±0.08 K [43].

4. Results and discussion

4.1. Wavelength-dependent, generalized temperature calibration function

Figure 4(a) shows the calibration data of eight RFBGs with nominal Bragg wavelengths at 1465 nm, 1485 nm, 1505 nm, 1525 nm, 1545 nm, 1565 nm, 1585 nm, and 1605 nm. This data set was used to design a generalized, wavelength-dependent calibration function. Therefore, polynomial functions of the form

$$\lambda_{B,j}(\vartheta) = \lambda_{0,j} + \sum\nolimits_{i=1}^{N} B_{i,j}\, \vartheta^{i} \tag{9}$$

with orders $N = 3,\ 4,\ 5,\ 6$, were fitted to the data of each RFBG ($j = 1..8$). To find the lowest degree of the polynomial that fits the wavelength vs. temperature data best, residuals of the measured wavelengths with the polynomial fit functions of various orders were considered. Figure 4(b) depicts the residuals for a 3rd order polynomial (blue circles), a 4th order polynomial (black crosses), and a 5th order polynomial (red pluses). The 3rd order fit shows a residual spread of ±7 pm and a systematic mismatch. The 4th order polynomial had considerably smaller residuals in the order of ±1 pm, but some systematic structure was still recognizable and similar was observed for the 5th order fit. The selection of the order of the fit function is further supported by evaluating the residual sum of squares (RSS), which is a typical measure to quantify the rationality of choice of a polynomial fit order. The RSS for the M samples of a single fit is given by [44]

$$RSS = \sum\nolimits_{k=1}^{M} (y_k - f(x_k))^2, \tag{10}$$

where y_k denotes the wavelength data point and $f(x_k)$ the associated point of the fit function. Figure 5 shows the RSS sorted according to the order of the polynomial fit for all 8 investigated RFBGs. No significant reduction of the RSS was observed for the 5th compared to the 4th order. Therefore, we decided to use 4th order polynomials for further data processing, as for the transition from 3rd to 4th order polynomials, the fit residuals and RSS improved significantly. Parameters of the 4th order fits are summarized in Table 2. Previous calibrations up to elevated temperatures greater than 700 °C showed sufficiency of 5th order polynomials [5,24,28,30,32] or 6th order polynomials [17,18].

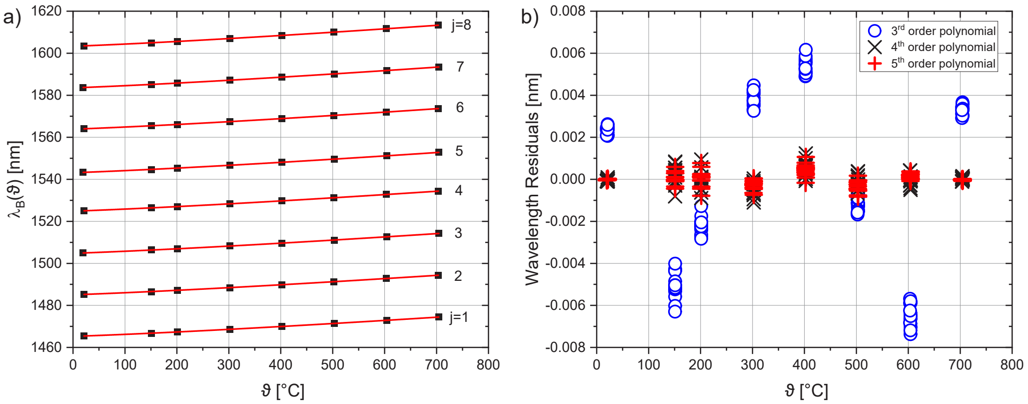

Fig. 4. a) Bragg wavelengths of the calibration measurements (black rectangles) and fits of 4th order polynomial functions (red lines) for each j-th RFBG sensor. b) Residuals of the fits with 3rd order (blue circles), 4th order (black crosses), and 5th order (red pluses) polynomials.

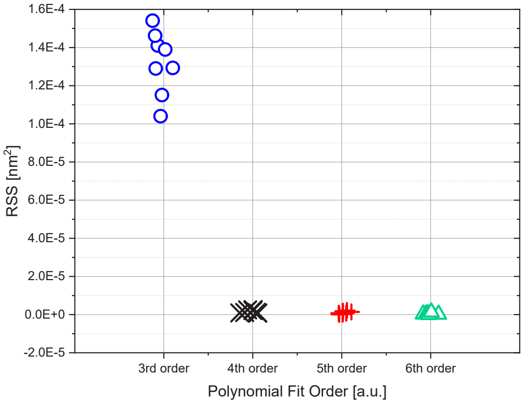

Fig. 5. Residual sum of squares (RSS) according to the order of the polynomial function used to fit the data. The RSS of all 8 sensors per category is shown. The transition from 3rd to 4th order improved the RSS significantly.

Table 2. Summary of fit coefficients $B_{i,j}$ and $\lambda_{0,j}$ of the 4th order polynomial temperature calibration functions for the 8 calibrated RFBG temperature sensors with different offset wavelengths.

j	$\lambda_{0,j}$	$B_{1,j}$	$B_{2,j}$	$B_{3,j}$	$B_{4,j}$
1	1465.242	8.80E-03	1.00E-05	−7.80E-09	3.01E-12
2	1485.041	8.94E-03	9.98E-06	−7.46E-09	2.74E-12
3	1504.766	9.04E-03	1.04E-05	−8.13E-09	3.14E-12
4	1524.822	9.15E-03	1.04E-05	−8.02E-09	3.05E-12
5	1543.109	9.27E-03	1.07E-05	−8.42E-09	3.28E-12
6	1563.837	9.39E-03	1.07E-05	−8.29E-09	3.16E-12
7	1583.494	9.56E-03	1.06E-05	−7.86E-09	2.82E-12
8	1603.291	9.64E-03	1.09E-05	−8.43E-09	3.23E-12

In the next step, the temperature-induced wavelength shifts $\Delta\lambda_{B,j}(\vartheta)$ of the RFBGs

$$\Delta\lambda_{B,j}(\vartheta) = \lambda_{B,j}(\vartheta) - \lambda_{0,j} = \sum\nolimits_{i=1}^{4} B_{i,j}\,\vartheta^{i}, \tag{11}$$

were calculated, where $B_{i,j}$ are the individual fit coefficients and $\lambda_{0,j}$ are the offset wavelengths at 0 °C of the j-th RFBG temperature sensor. The results are graphically represented in Fig. 6(a) with the wavelength shift data points (black rectangles) and 4th order polynomial fits (red lines). The calibration data ran apart with increasing temperature, indicating varying temperature sensitivities for different gratings with different offset wavelengths $\lambda_{0,j}$. A closer investigation of Fig. 6(b) shows that the calibration data arranged with respect to the offset wavelength $\lambda_{0,j}$ from low to high. For instance, at a fixed wavelength shift of 9.2 nm, the temperature deviation corresponds to ~50 K for the RFBGs at the lowest and highest offset wavelength $\lambda_{0,j}$. The temperature calibration of RFBGs over a broad spectral range demonstrated that a dependence on the offset wavelength must be considered for the RFBG temperature coefficients and the corresponding calibration curves.

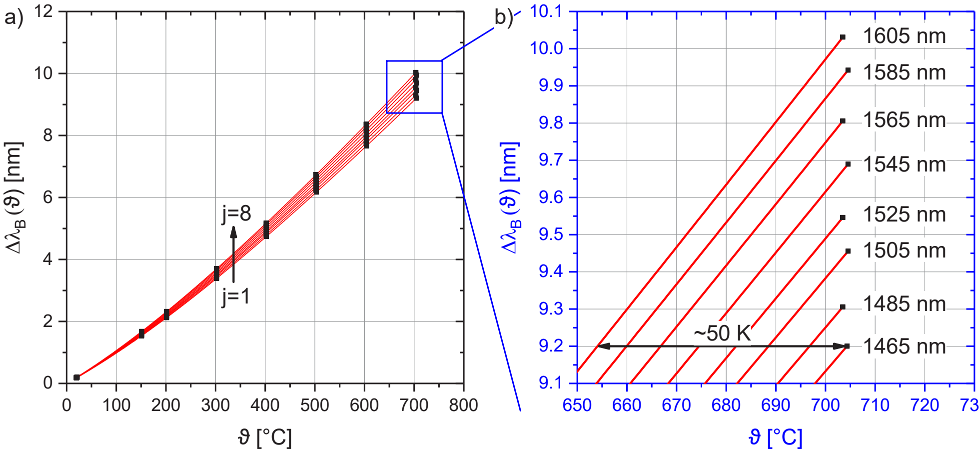

Fig. 6. a) Temperature-induced wavelength shifts. Each curve corresponds to a j-th sensor with varying offset wavelength $\lambda_{0,j}$ at 0 °C. Calibration data runs apart with increasing temperature, which leads to a wavelength-dependent temperature sensitivity of RFBG sensors of different offset wavelengths. b) Enlarging the area around 700 °C indicates that the calibration curves sort properly among their offset wavelengths $\lambda_{0,j}$.

The left column of Fig. 7, i.e., Figs. 7(a), 7(c), 7(e), and 7(g), show the 4th order polynomial fit coefficients $B_{i,j}$ as functions of each sensor's individual offset wavelength $\lambda_{0,j}$. Error bars denote the uncertainties of the polynomial fit coefficients. In particular, the linear fit coefficient $B_{1,j}$ shows a pronounced linear dependence with wavelength and the higher order coefficients show less dependence.

Additionally, linear fits to the $B_{i,j}$ parameters are depicted as red lines in the graphs. The observed linear wavelength dependencies gave reason to calculate wavelength-normalized fit coefficients $\tilde{B}_{i,j}$, as given by

$$\tilde{B}_{i,j} = \frac{B_{i,j}}{\lambda_{0,j}}. \tag{12}$$

These coefficients are depicted as functions of offset wavelength in the right column of Fig. 7, i.e., Figs. 7(b), 7(d), 7(f), and 7(h). These wavelength-normalized coefficients $\tilde{B}_{i,j}$. seem uncorrelated with the offset wavelengths and have only a small remaining spread of data points.

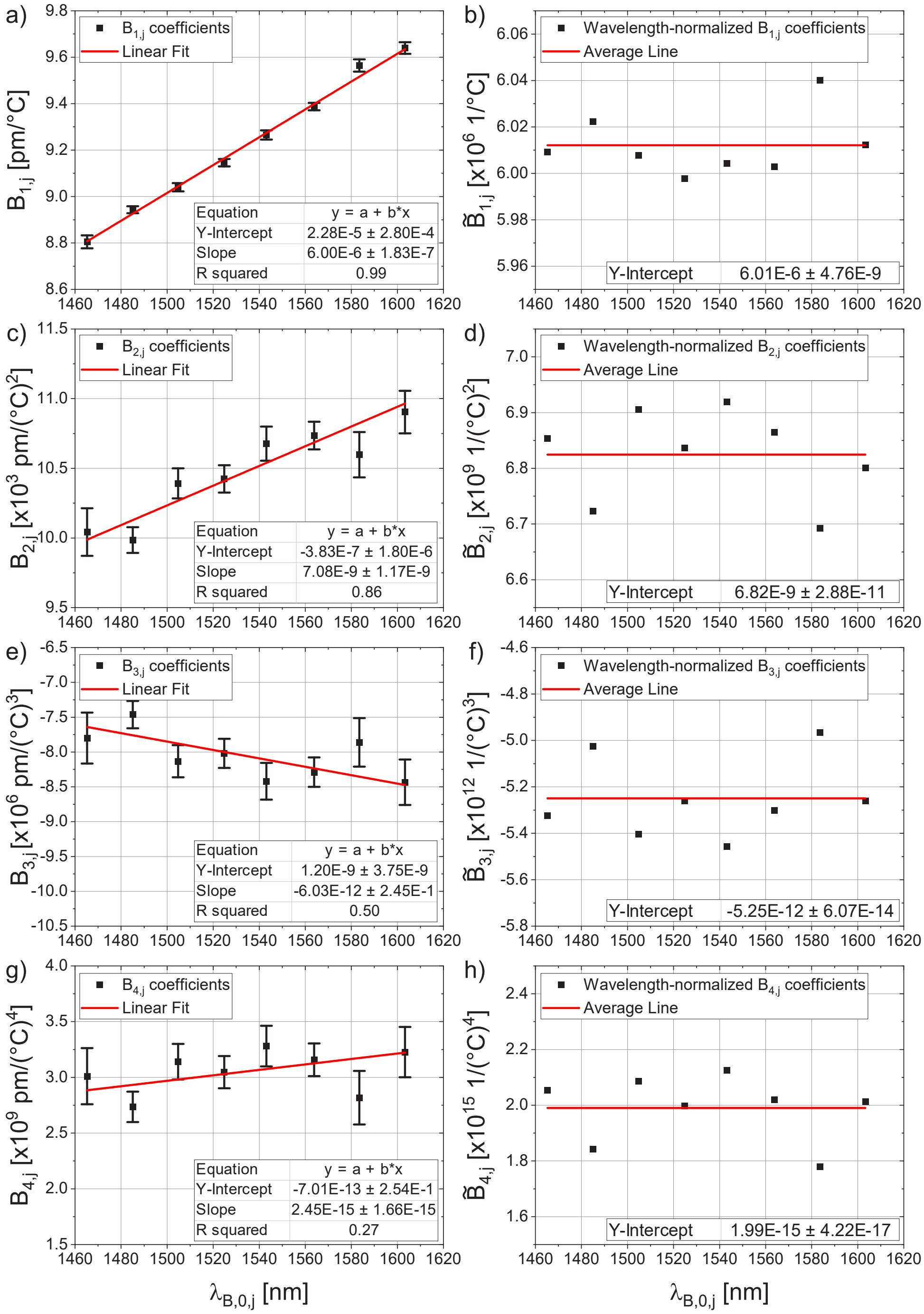

Fig. 7. Fit coefficients as functions of offset wavelengths $\lambda_{0,j}$ for a) $B_{1,j}$, c) $B_{2,j}$, e) $B_{3,j}$, and g) $B_{4,j}$. Linear fits (red lines) indicate linear correlations between wavelength and temperature, becoming less significant for higher order coefficients. Wavelength-normalized fit coefficients b) $\tilde{B}_{1,j}$, d) $\tilde{B}_{2,j}$, f) $\tilde{B}_{3,j}$, and h) $\tilde{B}_{4,j}$ show no significant dependence on wavelength. Averages over all 8 RFBGs (red horizontal lines) give representative wavelength-normalized calibration coefficients.

The independence of the coefficients to wavelength justifies averaging the values from all $j. = 1..8$ gratings, leading to the wavelength-normalized fit coefficients

$$\bar{B}_i = \frac{1}{N} \sum\nolimits_{j=1}^{N=8} \tilde{B}_{i,j}, \tag{13}$$

which are indicated as red horizontal lines in the charts of Figs. 7(b), d, f, h and summarized in Table 3. The value of $\bar{B}_1$ being 01×10^{-6} 1/°C can be physically interpreted as the sum of TOC and CTE and is consistent with literature [3].

Table 3. Wavelength-normalized standard calibration coefficients obtained for the generalized wavelength-dependent calibration function of identically fabricated RFBG temperature sensors.

Coefficient:	$\bar{B}_1$	$\bar{B}_2$	$\bar{B}_3$	$\bar{B}_4$
Unit:	$(°\mathrm{C})^{-1}$	$(°\mathrm{C})^{-2}$	$(°\mathrm{C})^{-3}$	$(°\mathrm{C})^{-4}$
Value:	6.01E-06	6.82E-09	−5.25E-12	1.99E-15

Using these averaged, wavelengtnormalized coefficients $\bar{B}_i$ for a 4th order polynomial function leads to a generalized, wavelength-dependent calibration function for any RFBG sensor element

$$\lambda_{B_{\lambda_0}}(\vartheta, \lambda_0) = \lambda_0 + \Delta\lambda_{B_{\lambda_0}}(\vartheta, \lambda_0) = \lambda_0 \left[1 + \sum\nolimits_{i=1}^{4} \bar{B}_i \, \vartheta^i\right], \tag{14}$$

where the only individual sensor parameter is the 0 °C offset wavelength λ_0. The new suffix 'λ_0' denotes the generality for gratings with any offset wavelength λ_0, as far as the fabrication parameters were maintained. Derivation of λ_0 for any new RFBG sensor element without running through a complete calibration cycle and the transferability of the standard calibration function to new sensors is discussed in Section 4.2.

4.2. Verification of the wavelength-dependent, generalized calibration function

Experimental verification of the generalized wavelength-dependent calibration function was accomplished with seven additional RFBG temperature sensors ($k = 1..7$) at the nominal wavelengths 1475 nm, 1495 nm, 1515 nm, 1535 nm, 1555 nm, 1575 nm, and 1595 nm. A single-point calibration of the 0 °C offset wavelength $\lambda_{0,k}$ was sufficient to apply the standard calibration function to these RFBG sensor elements, comprising a measurement of $\lambda_{B,k}(\vartheta_R)$ at a stabilized reference temperature ϑ_R – for instance, at RT using the Peltier-driven device described in Section 3.2. Hence, $\lambda_{0,k}$ can be calculated according to

$$\lambda_{0,k} = \lambda_{B,k}(\vartheta_R) \left[1 - \sum\nolimits_{i=1}^{4} \bar{B}_i \, \vartheta_R^i\right].. \tag{15}$$

With the knowledge of $\lambda_{0,k}$ and $\bar{B}_i$, the RFBG temperature sensors were ready for operation.

The new sensors were again placed in the calibration furnace and ran through a full calibration cycle, as described in Section 3b. This delivered individual wavelength data $\lambda_{B,k}(\vartheta)$ at temperatures ϑ for each sensor in the range from RT to 700 °C. Utilizing a numerical inversion of the standard calibration function in Eq. (14), the measured individual wavelength shifts $\Delta\lambda_{B,\lambda_{0,k}}(\vartheta) = \lambda_{B,k}(\vartheta) - \lambda_{0,k}$ re used to calculate the corresponding temperatures $\vartheta_{\lambda_{0,k}}$. The suffix '$\lambda_{0,k}$' denotes that the temperatures were calculated with the generalized, wavelength-dependent calibration function for the k-th RFBG with offset wavelength $\lambda_{0,k}$.

Figure 8 shows the difference between temperatures measured with the reference TC, ϑ, and the calculated RFBG temperatures $\vartheta_{\lambda_{0,k}}$ as a function of temperature ϑ in the furnace. The largest spread occurred at 700 °C with ±1.36 K. Nonetheless, depicted as black dashed lines is the lower and upper limit of the allowed uncertainty according to European standard IEC 60584 Class 1 for non-calibrated conventional thermocouples (TC), which is defined as ±1.5 K or ±0.4% of the temperature measurement value [1]. All RFBG sensors lay within the specified uncertainty, denoting that RFBG temperature sensors in combination with the generalized calibration complies with this standard, even under application of all assumptions and simplifications.

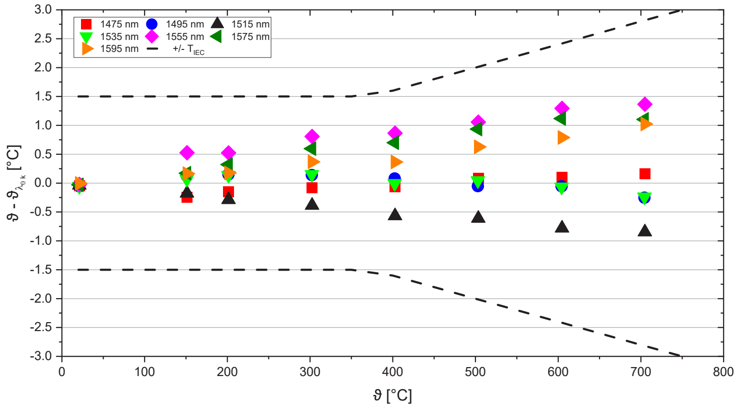

Fig. 8. Difference between temperatures of the calibration furnace, as measured by the calibrated thermocouple, ϑ, and RFBG temperatures $\vartheta_{\lambda_{0,k}}(\Delta\lambda_{B,k})$ calculated using the generalized, wavelength-dependent calibration function. Black dashed lines denote the lower and upper limit according to the European standard IEC 60584 Class 1 for non-calibrated conventional TCs [1], which verifies the suitability of proposed novel calibration procedure.

In Fig. 8, the data points of the respective RFBGs show systematic deviations, making it clear that the generalized calibration function found here is only an approximation for these sensors. Causes for these deviations may be due, on the one hand, to the simplifications made for Eq. (8), such as the wavelength dependence of the confinement factor, and on the other hand to unintended variations in the manufacturing parameters. Therefore, careful control of all production parameters is mandatory for this approach to ensure the achieved measurement precision between reference and calculated temperatures shown in Fig. 8. Nonetheless, performing only a single calibration at a reference temperature close to room temperature instead of running through a complete calibration between RT and 700 °C underlines a significant advantage. This is particularly important for multiplexed RFBG arrays that are spatially extended over lengths of more than several meters because, for these extended fiber-optic sensors, the realization of accurate calibration systems covering the entire length and the full temperature range up to ~700 °C is challenging, expensive, and practically barely feasible.

5. Conclusion

A novel temperature calibration scheme for RFBGs was introduced and carefully characterized using 8 identically fabricated RFBGs with different nominal Bragg wavelengths in the spectral band from 1465 nm to 1605 nm. FBG fabrication included writing the seed gratings and thermal annealing, where special emphasis was given to keep all fabrication parameters constant throughout sensor production. The impact of the variation of fabrication parameters, such as grating length, grating strength or annealing temperatures on the calibration precision and wavelength drift has not been investigated but will be subject of future research.

The RFBGs were exposed to heating cycles with temperature steps between RT and 700 °C to analyze the wavelength vs. temperature relationship. The most remarkable effect of each of the 8 RFBGs was a different, wavelength-dependent temperature response. A generalized calibration function that was proportional to the product of the RFBG wavelength at 0 °C, the so-called offset-wavelength and a 4^{th} order polynomial function of temperature were established. Combined with a one-point calibration at a given reference temperature, this generalized, wavelength-dependent calibration function could handle the temperature characteristics of identically fabricated RFBG sensors at different Bragg wavelengths.

Verification of this procedure was achieved using another 7 RFBGs, produced in the same wavelength range and with similar parameters. After exposing the RFBGs again to temperature cycles between RT and 700 °C, we could compare the reference temperature measured by a calibrated thermocouple, with the calculated temperatures using the generalized calibration curve. This investigation revealed only small deviations and demonstrated compliance with the European standard IEC 60584 Class 1 for non-calibrated conventional TCs.

It can be expected that this new calibration procedure could also be applied to fs-FBGs. Moreover, the effort to calibrate FBG sensor arrays with large spatial extend is dramatically reduced due to the restriction to a single calibration measurement at a reference temperature. Although further reduction of drift is an ongoing issue, presented results of this study suggest high-temperature stable multipoint FBGs as practical devices for real-world industrial temperature sensing.

Funding. Bundesministerium für Wirtschaft und Energie (03EE5041B).

Disclosures. The authors declare no conflicts of interest.

Data availability. Data underlying the results presented in this paper are not publicly available at this time but may be obtained from the authors upon reasonable request.

References

1. International Electrotechnical Commission, *IEC 60584-1. Thermocouples - Part 1: EMF specifications and tolerances* (IEC).
2. VDI/VDE 2660 Blatt 2:2020-04, *Technical temperature measurement - Optical temperature sensor based on fibre Bragg gratings - Recommendation on temperature measurement and statement of measurement uncertainty* (2660) (Beuth Verlag GmbH, 2020), https://www.beuth.de/en/technical-rule/vdi-vde-2660-blatt-2/292179575.
3. K. O. Hill and G. Meltz, "Fiber Bragg grating technology fundamentals and overview," J. Lightwave Technol. **15**(8), 1263–1276 (1997).
4. L. Polz, F. J. Dutz, R. R. Maier, H. Bartelt, and J. Roths, "Regenerated Fibre Bragg Gratings: A critical assessment of more than 20 years of investigations," Opt. Laser Technol. **134**, 106650 (2021).
5. F. J. Dutz, A. Heinrich, R. Bank, A. W. Koch, and J. Roths, "Fiber-Optic Multipoint Sensor System with Low Drift for the Long-Term Monitoring of High-Temperature Distributions in Chemical Reactors," Sensors **19**(24), 5476 (2019).
6. S. J. Mihailov, "Fiber Bragg grating sensors for harsh environments," Sensors **12**(2), 1898–1918 (2012).
7. S. Yang, D. Hu, and A. Wang, "Point-by-point fabrication and characterization of sapphire fiber Bragg gratings," Opt. Lett. **42**(20), 4219–4222 (2017).
8. J. Thomas, C. Voigtländer, R. G. Becker, D. Richter, A. Tünnermann, and S. Nolte, "Femtosecond pulse written fiber gratings: a new avenue to integrated fiber technology," Laser Photonics Rev. **6**(6), 709–723 (2012).
9. S. J. Mihailov, C. Hnatovsky, N. Abdukerim, R. B. Walker, P. Lu, Y. Xu, X. Bao, H. Ding, M. de Silva, D. Coulas, and D. Grobnic, "Ultrafast Laser Processing of Optical Fibers for Sensing Applications," Sensors **21**(4), 1447 (2021).
10. D. Grobnic, C. Hnatovsky, S. Dedyulin, R. B. Walker, H. Ding, and S. J. Mihailov, "Fiber Bragg Grating Wavelength Drift in Long-Term High Temperature Annealing," Sensors **21**(4), 1454 (2021).
11. N. Jovanovic, J. Thomas, R. J. Williams, M. J. Steel, G. D. Marshall, A. Fuerbach, S. Nolte, A. Tünnermann, and M. J. Withford, "Polarization-dependent effects in point-by-point fiber Bragg gratings enable simple, linearly polarized fiber lasers," Opt. Express **17**(8), 6082–6095 (2009).
12. R. J. Williams, N. Jovanovic, G. D. Marshall, G. N. Smith, M. J. Steel, and M. J. Withford, "Optimizing the net reflectivity of point-by-point fiber Bragg gratings: the role of scattering loss," Opt. Express **20**(12), 13451–13456 (2012).
13. F. J. Dutz, S. Boje, U. Orth, A. W. Koch, and J. Roths, "High-Temperature Profile Monitoring in Gas Turbine Exhaust-Gas Diffusors with Six-Point Fiber-Optic Sensor Array," IJTPP **5**(4), 25 (2020).
14. F. Dutz, M. Lindner, A. Heinrich, C. G. Seydel, T. Bosselmann, A. W. Koch, and J. Roths, "Multipoint high temperature sensing with regenerated fiber Bragg gratings," in *Fiber Optic Sensors and Applications XV* (SPIE, 2018), p. 6.
15. R. B. Walker, S. Yun, M. de Silva, N. Charest, D. Robertson, S. Mihailov, C. Hnatovsky, P. Lu, and P. Vena, "High temperature measurement of a low emission, high pressure combustor using femtosecond laser written fiber Bragg gratings," in *Fiber Optic Sensors and Applications XV* (SPIE, 2018), p. 7.
16. R. B. Walker, S. Yun, H. Ding, M. Charbonneau, D. Coulas, N. Ramachandran, and S. J. Mihailov, "High-resolution fast temperature mapping of a gas turbine combustor simulator with femtosecond infrared laser written fiber Bragg gratings," in *Photonic Instrumentation Engineering IV*, SPIE Proceedings (SPIE, 2017), 101101 H.

17. R. B. Walker, H. Ding, D. Coulas, D. Grobnic, S. J. Mihailov, M. A. Duchesne, R. W. Hughes, D. J. McCalden, and R. Burchat, "Entrained-flow gasifier and fluidized-bed combustor temperature monitoring using arrays of fs-IR written fiber Bragg gratings," in *24th International Conference on Optical Fibre Sensors*, SPIE Proceedings (SPIE, 2015), 96343X.
18. R. B. Walker, H. Ding, D. Coulas, D. Grobnic, P. Lu, S. J. Mihailov, M. A. Duchesne, R. W. Hughes, D. J. McCalden, R. Burchat, and R. Yandon, "High temperature monitoring of an oxy-fuel fluidized bed combustor using femtosecond infrared laser written fiber Bragg gratings," in *Photonic Instrumentation Engineering III*, SPIE Proceedings (SPIE, 2016), p. 975413.
19. R. Rodríguez-Garrido, A. Carballar, J. Vera, J. González-Aguilar, A. Altamirano, A. Loureiro, and D. Pereira, "High-Temperature Monitoring in Central Receiver Concentrating Solar Power Plants with Femtosecond-Laser Inscribed FBG," Sensors **21**(11), 3762 (2021).
20. H. Xia, "Advanced fiber optical sensor and instrumentation for power generation industrial monitoring and diagnostics," Proc. SPIE **8370**, 83700F 2012).
21. H. Xia, D. Byrd, S. Dekate, and B. Lee, "High-Density Fiber Optical Sensor and Instrumentation for Gas Turbine Operation Condition Monitoring," J. Sens. **2013**, 1–10 (2013).
22. M. A. S. Zaghloul, M. Wang, S. Huang, C. Hnatovsky, D. Grobnic, S. Mihailov, M.-J. Li, D. Carpenter, L.-W. Hu, J. Daw, G. Laffont, S. Nehr, and K. P. Chen, "Radiation resistant fiber Bragg grating in random air-line fibers for sensing applications in nuclear reactor cores," Opt. Express **26**(9), 11775–11786 (2018).
23. Z. Wu, M. A. S. Zaghloul, D. Carpenter, M.-J. Li, J. Daw, Z.-H. Mao, C. Hnatovsky, S. J. Mihailov, and K. P. Chen, "Mitigation of Radiation-Induced Fiber Bragg Grating (FBG) Sensor Drifts in Intense Radiation Environments Based on Long-Short-Term Memory (LSTM) Network," IEEE Access **9**, 148296–148301 (2021).
24. N. Chanet, Y. Corre, R. Cotillard, J. Gaspar, G. Laffont, C. Pocheau, G. Caulier, C. Dechelle, B. de Gentile, C. Destouches, L. Dubus, F. Gallay, C. Hernandez, M. Missirlian, M. Richou, N. Roussel, and B. Santraine, "Design and integration of femtosecond Fiber Bragg gratings temperature probes inside actively cooled ITER-like plasma-facing components," Fusion Eng. Des. **166**, 112376 (2021).
25. Y. Corre, N. Chanet, R. Cotillard, J. Gaspar, G. Laffont, C. Pocheau, G. Caulier, C. Destouches, J.-L. Gardarein, M. Firdaouss, M. Houry, M. Missirlian, N. Roussel, and B. Santraine, "First temperature database achieved with Fiber Bragg Grating sensors in uncooled plasma facing components of the WEST lower divertor," Fusion Eng. Des. **170**, 112528 (2021).
26. G. Laffont, R. Cotillard, P. Ferdinand, J.-P. Jeannot, and G. Rodriguez, eds., *Regenerated Fiber Bragg Grating sensors for high temperature monitoring in Sodium-cooled Fast Reactor* (2015).
27. G. Laffont, R. Cotillard, N. Roussel, R. Desmarchelier, and S. Rougeault, "Temperature Resistant Fiber Bragg Gratings for On-Line and Structural Health Monitoring of the Next-Generation of Nuclear Reactors," Sensors **18**(6), 1791 (2018).
28. Y. Corre, G. Laffont, C. Pocheau, R. Cotillard, J. Gaspar, N. Roussel, M. Firdaouss, J.-L. Gardarein, D. Guilhem, and M. Missirlian, "Integration of fiber Bragg grating temperature sensors in plasma facing components of the WEST tokamak," Rev. Sci. Instrum. **89**(6), 063508 (2018).
29. Q. Bian, A. Podhrazsky, C. Bauer, A. Stadler, F. Buchfellner, R. Kuttler, M. Jakobi, W. Volk, A. Koch, and J. Roths, "Temperature and external strain sensing with metal-embedded optical fiber sensors for structural health monitoring," Opt. Express **30**(19), 33449 (2022).
30. M. Lindner, E. Tunc, K. Weraneck, F. Heilmeier, W. Volk, M. Jakobi, A. W. Koch, and J. Roths, "Regenerated Bragg Grating Sensor Array for Temperature Measurements During an Aluminum Casting Process," IEEE Sensors J. **18**(13), 5352–5360 (2018).
31. M. Lindner, A. Stadler, G. Hamann, B. Fischer, M. Jakobi, F. Heilmeier, C. Bauer, W. Volk, A. W. Koch, and J. Roths, "Fiber Bragg Sensors Embedded in Cast Aluminum Parts: Axial Strain and Temperature Response," Sensors **21**(5), 1680 (2021).
32. Q. Bian, C. Bauer, A. Stadler, M. Lindner, M. Jakobi, W. Volk, A. W. Koch, and J. Roths, "In-situ High Temperature and Large Strain Monitoring during a Copper Casting Process based on Regenerated Fiber Bragg Grating Sensors," J. Lightwave Technol. **39**(20), 6660–6669 (2021).
33. F. Juelich and J. Roths, "OP2 - Determination of the Effective Refractive Index of Various Single Mode Fibres for Fibre Bragg Grating Sensor Applications," in *Proceedings OPTO 2009 & IRS*^{2} *2009* (AMA Service GmbH, Von-Münchhausen-Str. 49, 31515 Wunstorf, Germany, 2009), pp. 119–124.
34. H. Gao, Y. Jiang, Y. Cui, L. Zhang, J. Jia, and L. Jiang, "Investigation on the Thermo-Optic Coefficient of Silica Fiber Within a Wide Temperature Range," J. Lightwave Technol. **36**(24), 5881–5886 (2018).
35. P. K. Bachmann, D. U. Wiechert, and T. P. M. Meeuwsen, "Thermal expansion coefficients of doped and undoped silica prepared by means of PCVD," J. Mater. Sci. **23**(7), 2584–2588 (1988).
36. M. Born, E. Wolf, A. B. Bhatia, P. C. Clemmow, D. Gabor, A. R. Stokes, A. M. Taylor, P. A. Wayman, and W. L. Wilcock, *Principles of Optics* (Cambridge University Press, 2013).
37. J. W. Fleming, "Dispersion in GeO_2-SiO_2 glasses," Appl. Opt. **23**(24), 4486 (1984).
38. B. J. Frey, D. B. Leviton, and T. J. Madison, "Temperature-dependent refractive index of silicon and germanium," in *Optomechanical Technologies for Astronomy*, SPIE Proceedings (SPIE, 2006), 62732J.
39. G. Ghosh, M. Endo, and T. Iwasaki, "Temperature-dependent Sellmeier coefficients and chromatic dispersions for some optical fiber glasses," J. Lightwave Technol. **12**(8), 1338–1342 (1994).

40. G. Ghosh, “Temperature dispersion of refractive indexes in some silicate fiber glasses,” IEEE Photonics Technol. Lett. **6**(3), 431–433 (1994).
41. C. Z. Tan, “Dependence of the refractive index on density, temperature, and the wavelength of the incident light,” Eur. Phys. J. B **94**(7), 139 (2021).
42. Klasmeier Kalibrier- und Messtechnik GmbH, *Kalibrierschein. Kalibrierzeichen D-K-15224-01-00* (2019).
43. TÜV SÜD Industrie Service GmbH, Kalibrierschein. Kalibrierzeichen D-K-14154-01 (2017).
44. I. Pardoe, *Applied regression modeling*, 3 edition (John Wiley & Sons, 2020).